nature communications

Article

https://doi.org/10.1038/s41467-024-53786-1

Synthesis and structure of a non-van-der-Waals two-dimensional coordination polymer with superconductivity

Received: 18 June 2024

Accepted: 17 October 2024

Published online: 29 October 2024

Check for updates

Zhichao Pan[1,2,14], Xing Huang[3,14], Yunlong Fan[1,2], Shaoze Wang[4], Yiyu Liu[5], Xuzhong Cong[6], Tingsong Zhang[7,8], Shichao Qi[9], Ying Xing[5], Yu-Qing Zheng[7,8], Jian Li[10], Xiaoming Zhang[11], Wei Xu[12], Lei Sun[4], Jian Wang[9,13] & Jin-Hu Dou[1,2]

Two-dimensional conjugated coordination polymers exhibit remarkable charge transport properties, with copper-based benzenehexathiol (Cu-BHT) being a rare superconductor. However, the atomic structure of Cu-BHT has remained unresolved, hindering a deeper understanding of the superconductivity in such materials. Here, we show the synthesis of single crystals of Cu_3BHT with high crystallinity, revealing a quasi-two-dimensional kagome structure with non-van der Waals interlayer Cu-S covalent bonds. These crystals exhibit intrinsic metallic behavior, with conductivity reaching 10^3 S/cm at 300 K and 10^4 S/cm at 2 K. Notably, superconductivity in Cu_3BHT crystals is observed at 0.25 K, attributed to enhanced electron-electron interactions and electron-phonon coupling in the non-van der Waals structure. The discovery of this clear correlation between atomic-level crystal structure and electrical properties provides a crucial foundation for advancing superconductor coordination polymers, with potential to revolutionize future quantum devices.

Two-dimensional conjugated coordination polymers (2D c-CPs) and conjugated metal-organic frameworks (2D c-MOFs) are emerging as a novel type of electronic materials[1–4]. They are functional materials with a 2D periodic network structure formed by the self-assembly of metal centers and organic ligands through coordination bonds[5–7]. These materials are characterized by electron-rich conjugated ligands, such as benzenehexathiolate (BHT)[8–12], hexaiminobenzene (HIB)[13,14], 2,3,6,7,10,11-hexahydroxytriphenylene (HHTP)[15–17], 2,3,6,7,10,11-hexaaminotriphenylene (HITP)[18–20] and others, along with transition metal-centered coordination modes[21,22]. The unique 2D π-d conjugation

[1]National Key Laboratory of Advanced Micro and Nano Manufacture Technology, School of Materials Science and Engineering, Peking University, Beijing 100871, China. [2]Key Laboratory of Polymer Chemistry and Physics of Ministry of Education, School of Materials Science and Engineering, Peking University, Beijing 100871, China. [3]Center for Advancing Electronics Dresden & Faculty of Chemistry and Food Chemistry, Technische Universität Dresden, Dresden 01062, Germany. [4]Department of Chemistry and Department of Physics, School of Science, Westlake University, Hangzhou 310030, China. [5]State Key Laboratory of Heavy Oil Processing, College of New Energy and Materials, China University of Petroleum, Beijing 102249, China. [6]College of Chemistry and Molecular Engineering, Peking University, Beijing 100871, China. [7]National Key Laboratory of Advanced Micro and Nano Manufacture Technology, School of Integrated Circuits, Peking University, Beijing 100871, China. [8]Beijing Advanced Innovation Center for Integrated Circuits, School of Integrated Circuits, Peking University, Beijing 100871, China. [9]International Center for Quantum Materials, School of Physics, Peking University, Beijing 100871, China. [10]School of Chemistry and Chemical Engineering, Nanjing University, Nanjing 210093, China. [11]College of Physics and Optoelectronic Engineering, Ocean University of China, Qingdao, Shandong 266100, China. [12]Beijing National Laboratory for Molecular Sciences, Key Laboratory of Organic Solids, Institute of Chemistry Chinese Academy of Sciences, Beijing 100190, China. [13]Collaborative Innovation Center of Quantum Matter, Beijing 100871, China. [14]These authors contributed equally: Zhichao Pan, Xing Huang. e-mail: doujinhu@pku.edu.cn

electronic structure grants them excellent charge transport properties[8], which challenges the conventional belief that CPs and MOFs are poor electron conductors[23]. The excellent charge transport properties and unique programmable topology and composition of 2D c-CPs offer a rich framework for exploring various exotic condensed-matter physics, including topological insulators[24–26], spin lattices[27], quantum spin liquid[28], Weyl semimetals[29], superconductivity[10,30,31], etc.

Unlike charge-transfer complex organic superconductors, 2D c-MOFs form conductive pathways via in-plane *π-d* interactions, involving both through-bond and extended conjugation mechanisms[3]. The introduction of metal ions facilitates the creation of in-plane *π-d* conductive channels, potentially amplifying electron–electron interactions and thus promoting superconductivity. Cu-BHT stands as the sole superconductor amidst the expansive realm of CPs and MOFs, yet exists as a powder sample without precise atomic structure characterization[10,30]. Pellets or multi-crystalline films are susceptible to external factors such as impurities, random crystal orientation, grain boundaries, and defects, complicating the precise atomic-scale structure determination of Cu_3BHT and impeding a comprehensive understanding of its intrinsic electrical characteristics and superconductivity behavior. The lack of atomic-resolution crystal structure of Cu_3BHT also hinders theoretical investigation of the nature of its superconductivity[10,30]. Overcoming these challenges is crucial for establishing the theoretical groundwork needed to propel the advancement of novel CPs and MOFs-based superconductors.

In this work, to address this challenge, micro-crystal arrays of Cu_3BHT were realized through liquid-liquid interface reactions, yielding the highest crystallinity and largest single crystals among Cu-BHT materials. High-quality single crystals allow atomic-precision structural determination, which revealed a quasi-2D kagome structure with non-van der Waals interactions, characterized by robust interlayer interactions mediated through Cu–S covalent bonds. This finding contrasts sharply with the previously assumed graphite-like layered structure and provides the first proof of Cu_3BHT 's exact atomic arrangement. Single-crystal devices were fabricated to reveal the interlayer charge transport properties of Cu_3BHT. Cu_3BHT shows an intrinsic metallic behavior with electrical conductivity reaching 10^3 S/cm at room temperature and 10^4 S/cm at 2 K. Most notably, Cu_3BHT single-crystal devices exhibit a superconductivity transition at 0.25 K. Furthermore, theoretical calculations have further elucidated the superconducting mechanism in Cu_3BHT, attributed to the enhanced its electron–phonon coupling and electron–electron interaction, which are induced by its distinctive kagome structure and interlayer Cu–S bonds. This clear illustration of the electrical properties' origin for Cu_3BHT represents a significant advancement in the field of c-CPs and MOFs, offering new insights into the design and engineering of functional c-CPs-based quantum materials and devices.

Results

Synthesis of Cu_3BHT micro-crystal array

Micro-crystal arrays of Cu_3BHT were prepared through interfacial self-assembly between a toluene solution of ligand and an aqueous solution of the Cu source. The crystallinity of 2D c-CPs is closely associated with reaction reversibility[32]. Especially, higher reaction temperatures can make the coordination reaction more reversible[33,34]. Dichloromethane is the most common solvent choice for interfacial synthesis of 2D c-CPs[8,10]. However, its low boiling point limits the achievable reaction temperatures, thereby constraining the reversibility of the reaction and the concentration of the ligand. To overcome these challenges, we substituted dichloromethane with toluene, a solvent with a higher boiling point. Our synthesis trials revealed that temperature and precursor concentration are critical factors influencing the sizes of Cu_3BHT crystals. Controlled crystal growth was achieved by reacting a 1.85 mmol/L toluene solution of the ligand and a 2×10^{-2} mol/L $CuCl_2$ aqueous solution at 75 °C for 1 week, as shown in Supplementary Figs. 1–4.

The scanning electron microscopy (SEM) image presented in Fig. 1d illustrates that highly oriented micro-crystal is densely packed in the Cu_3BHT film. These crystals are significantly larger than those reported in previous studies[8], with lengths reaching several micrometers and a cross-sectional area exceeding 10^4 nm^2. Additionally, phase-pure single crystals of Cu_3BHT, which are suitable for both the single structure determination and single-crystal device fabrication, can now be efficiently produced through simple ultrasonication of Cu_3BHT micro-crystal arrays.

The powder X-ray diffraction (PXRD) patterns and Raman spectra of the synthesized Cu_3BHT demonstrate markedly improved quality over previous studies[8,10], particularly with respect to the full width at half maximum (FWHM) and the significantly increased number of detectable peaks (Supplementary Figs. 5–7). These improvements in crystallinity are crucial for enhancing the resolution of structural determination for Cu_3BHT. The synchrotron PXRD ($\lambda = 0.458086$ Å) result of the meticulously grown Cu_3BHT samples is displayed in Fig. 1g. The sample's monoclinic crystal system is well-indexed, with unit cell parameters $a = 14.8082(10)$ Å, $b = 8.6706(6)$ Å, $c = 6.8357(5)$ Å, $\alpha = \gamma = 90°$ and $\beta = 97.342(2)°$. Notably, two closely spaced peaks at the lowest angle (3.51° and 3.57°, d-spacing = 7.4788 and 7.3531 Å) are indexed as (110) and (200), respectively. These peaks, corresponding to the in-plane hexagonal periodic packing, were indistinguishable in previous reports due to peak overlap[8,10]. This finding indicates that the in-plane structure of Cu_3BHT possesses a lower symmetry than a perfect hexagonal lattice.

Single crystal structure characterization of Cu_3BHT

The successful synthesis of high-quality crystals enabled the first atomic-resolution structure analysis of Cu_3BHT. High-resolution scanning transmission electron microscopy (HR-STEM) images revealed a 2D kagome lattice of Cu atoms in Cu_3BHT (Fig. 1e and Supplementary Fig. 8), which is consistent with previous reports[8,10,30]. Furthermore, the atomic-precision structure of Cu_3BHT was directly solved using the Microcrystal electron diffraction (Micro-ED) method in TEM with an *ab* initio approach. As shown in Fig. 1f, the structure of Cu_3BHT is depicted along the *c*-axis. The high resolution of the Micro-ED dataset, reaching up to 0.696 Å (indicated by the yellow circle), facilitated the direct location of all non-hydrogen atoms within the structure (Supplementary Fig. 9). In contrast, previous structure determinations of Cu_3BHT only reached a resolution of 2.3660 Å[10]. This structure was subsequently refined against high-resolution synchrotron PXRD data through Rietveld refinement. Our results indicate that Cu_3BHT crystallizes in the monoclinic $P2_1/c$ space group, indicating an ABAB double-layer stacking structure.

The single crystal structure of Cu_3BHT is depicted in Fig. 1. Each BHT ligand is surrounded by six Cu atoms, with Cu–S distances ranging from 2.26(1) to 2.33(9) Å (Supplementary Fig. 10). Each Cu atom is linked to two BHT ligands, forming a kagome lattice (Fig. 1a and Supplementary Fig. 11). Notably, the atomic-resolution structure has revealed a critical feature of Cu_3BHT that was previously overlooked. Unlike the commonly assumed van der Waals interactions and *π–π* interactions between layers in 2D c-CPs, Cu–S bonds (2.662(6) Å) are present to connect adjacent Cu_3BHT layers (Fig. 1b). The length of the Cu–S bonds reported here is similar to other Cu–S bonds that have been observed in the crystal structures of other materials[35,36]. There are two distinct coordination environments for Cu within Cu_3BHT. Specifically, two-thirds of the Cu atoms exhibit 4-coordination in a square planar geometry, whereas the remaining third are 5-coordinated, forming a square pyramidal structure. Similarly, the S atoms split into two-thirds μ2 and one-third μ3 categories. Although the average interlayer distance is 3.32 Å, a markedly shorter covalent contact of 2.66 Å occurs between the layers through Cu–S bonds. From another

https://doi.org/10.1038/s41467-024-53786-1

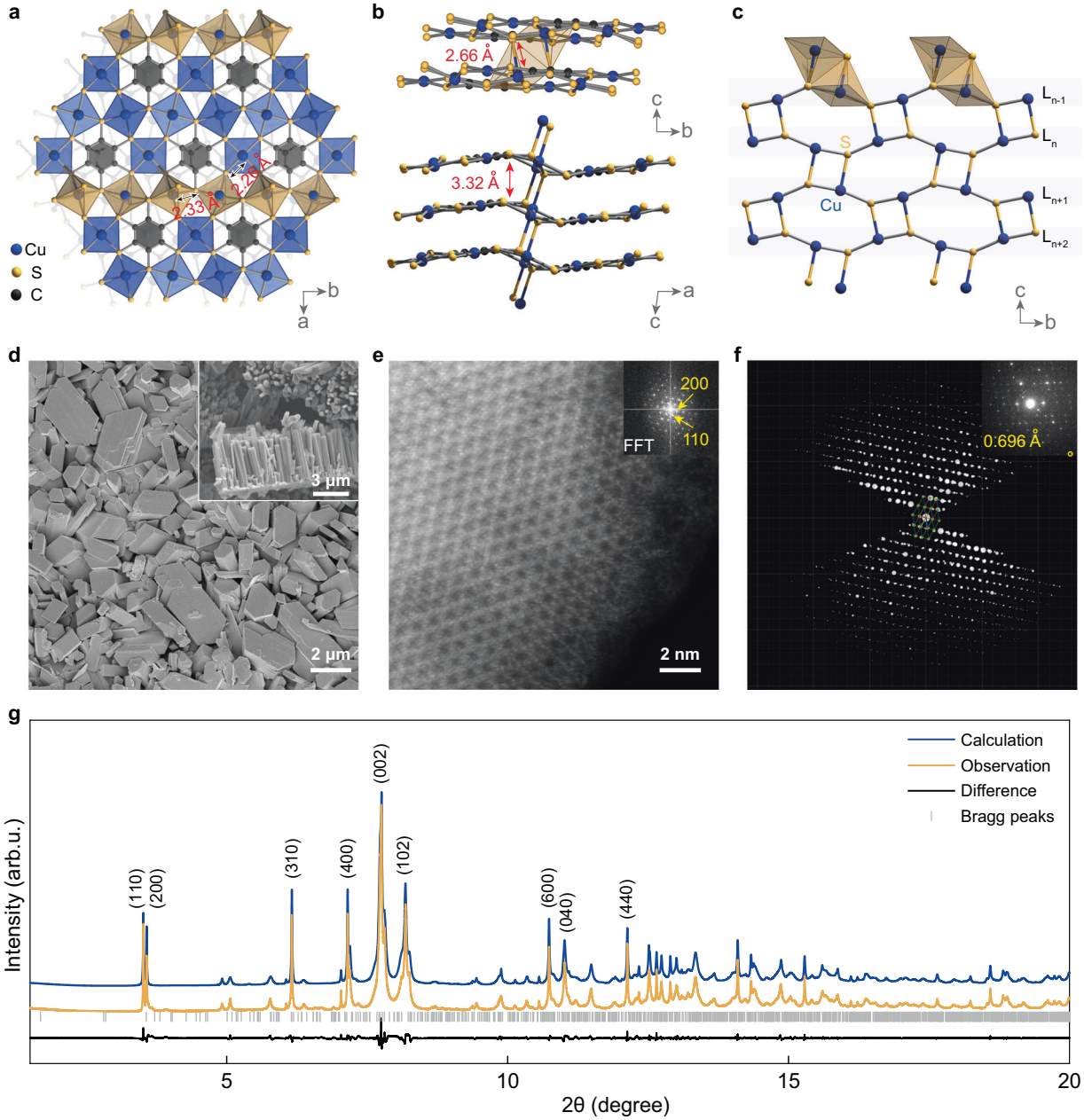

Fig. 1 | Single crystal structure of Cu_3BHT. a A representation of the crystal structure of Cu_3BHT viewed along the *c* direction. **b** The metal-ligand connectivity of the five-coordinate Cu atoms and layer stacking of Cu_3BHT. **c** The charge transport network formed by Cu–S bonds. **d** The SEM micrograph reveals that closely packed single crystals is formed in Cu_3BHT film. **e** HR-STEM image of Cu_3BHT (inset: fast Fourier transform (FFT) of the micrograph). **f** High-resolution Micro-ED data. **g** PXRD data of synthesized Cu_3BHT. Blue line: calculated intensities; orange line: observed intensities; gray line: Bragg peaks; black line: difference.

structural perspective, it can be seen as a Cu–S network of the 4.8.8 net, aligned with the (100) plane. The axial Cu–S bonds link the layers vertically, endowing Cu_3BHT with a distinctive non-van der Waals 2D structure that includes both a fully conjugated 2D plane and vertically oriented short covalent interactions between layers (Fig. 1c).

Single crystal device characterization

Four probe single-crystal devices were fabricated to reveal the intrinsic electrical properties of Cu_3BHT. The SEM image of the device (Fig. 2a) reveals that a typical Cu_3BHT crystal exhibits a rod-like morphology with an edge-on orientation. Four electrodes (5 nm Ti/250 nm Au) were deposited perpendicular to the long axis of the crystal, enabling the characterization of charge transport along the out-of-plane direction ([001] direction) (Supplementary Figs. 12–14). In Supplementary Fig. 13, the SEM image and elemental mapping confirm the structural integrity of the Cu_3BHT single-crystal device, with no visible cracks or boundary damage observed after electron beam lithography (EBL). This stability is attributed to the precise optimization of electron beam dosage, ensuring effective photoresist development while preserving the crystal structure. As indicated in Fig. 2b, the linear voltage-current behavior confirms the Ohmic contact, ensuring the reliability of electrical measurements. The negligible difference in conductivity between two-probe and four-probe measurements at room temperature confirms minimal contact resistance between Cu_3BHT and the electrodes. The electrical conductivity of Cu_3BHT along the out-of-plane direction is estimated to be approximately 10^3 S/cm at 300 K, increasing to 10^4 S/cm at 2 K (Fig. 2b, c).

https://doi.org/10.1038/s41467-024-53786-1

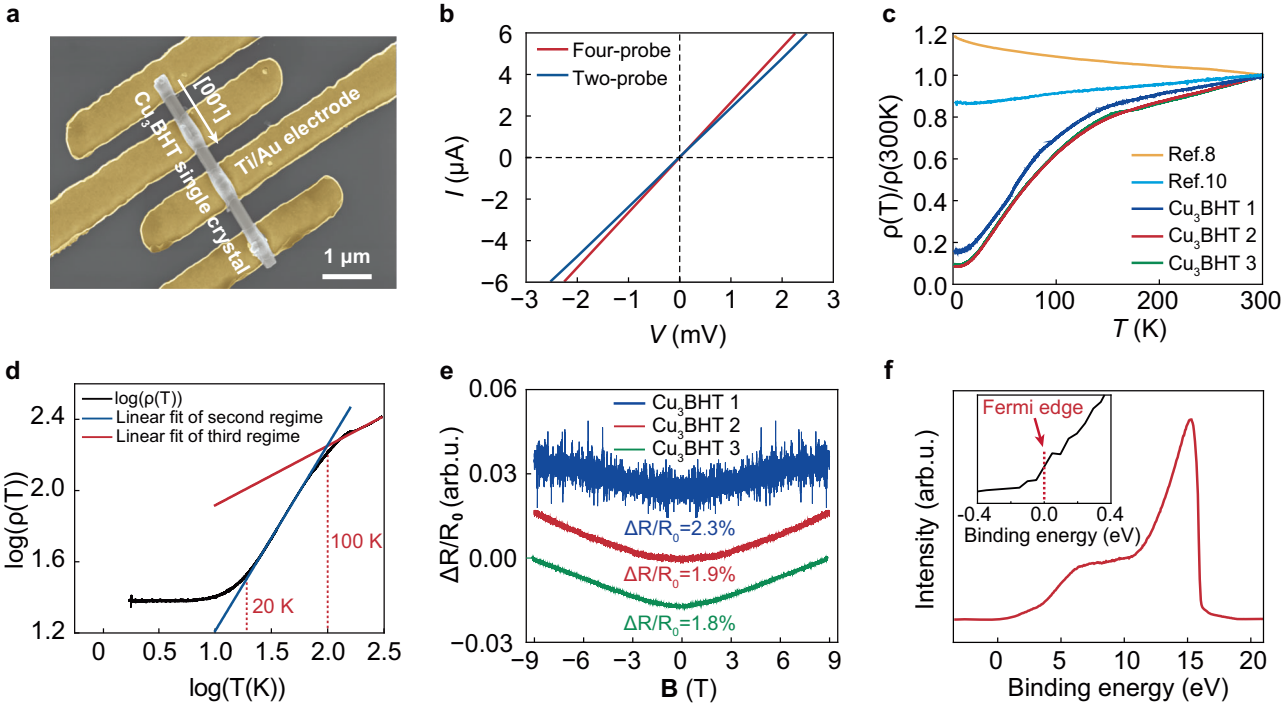

Fig. 2 | Electrical properties of Cu_3BHT. **a** The SEM image of a single crystal Cu_3BHT device. **b** Out-of-plane two-probe and four-probe *I*–*V* curves were measured from a Cu_3BHT single-crystal device at room temperature. **c** Four-probe temperature-dependent normalized resistivity of three single crystal devices and compared with previous reports. **d** log($\rho(T)$) vs log(T) for Cu_3BHT 2 at zero magnetic field. **e** The relationship between magnetic induction intensity and resistance change, with magnetic field orientation aligned with the current direction. **f** UPS data for the valence band region of Cu_3BHT were acquired at 300 K, and the Fermi edge is shown by the red dotted line.

The high interlayer conductivity may be attributed to van der Waals and π–π interactions, as well as the covalently bonded Cu–S network, as shown in the previous discussion (Fig. 1c). The interlayer Cu–S bonding may not only increase the efficiency of charge carrier transport but also stabilize the stacking structure, preventing the Peierls transition[37,38]. Figure 2c shows the temperature dependence of normalized out-of-plane resistivity ($\rho(T)/\rho(300\,K)$ vs T), with the residual-resistance ratio (RRR) value reaching up to 10, comparable to that of typical copper exposed to environmental conditions[39]. This is significantly higher than other metallic MOFs, which typically have RRR values close to 1[8,10], indicating the high quality of our Cu_3BHT crystal and its strong metallic behavior. The temperature-dependent resistivity and conductivity of the single-crystal devices were characterized using the four-probe method, as illustrated in Supplementary Figs. 15 and 16. Three devices were measured, and their results were compared with those previously reported poly-crystalline Cu-BHT samples[8,10]. All three single-crystal devices consistently demonstrated clear metallic behavior from 2 to 300 K. The measurements based on film samples are more sample-dependent (Supplementary Fig. 17). This is primarily due to the film samples containing numerous crystal boundaries and less precise control over crystal orientations, resulting in a mixture of intrinsic and extrinsic charge transport properties. In conclusion, our results provide a more intrinsic and detailed picture of the charge transport properties of Cu_3BHT.

The log(ρ) vs log(T) plot in Fig. 2d illustrates that the temperature dependence of Cu_3BHT can be divided into three distinct regimes. At very low temperatures (<10 K), the resistivity of Cu_3BHT shows minimal temperature dependence, marked by a pronounced minimum resistance value. This phenomenon may be attributed to the significant exchange coupling between the conduction electron gas and impurities (such as trace amounts of free Cu^{2+} ions), which induces a novel electronic state that stabilizes the resistivity. Between 20 and 100 K, the resistivity exhibits a linear temperature dependence, $\rho \propto T$, which can be attributed to the metallic charge transport behavior. This linear dependence is often regarded as a key indicator of non-Fermi-liquid behavior[40]. As the temperature rises, the amplitude of lattice vibrations escalates, consequently intensifying electron–phonon scattering. However, as temperatures surpass 100 K, the resistivity exhibits a power-law dependence, $\rho \propto T^{0.31}$. This change is likely due to the saturation of lattice vibrations and carrier scattering mechanisms, where the scattering probability ceases to increase significantly with temperature, leading to a slower rise in resistivity. The single-crystal device used in this study enables the exploration of complex metallic behaviors in 2D c-CPs that were previously unexplored.

The metallic properties of Cu_3BHT are supported by the results of magnetoresistance measurements shown in Fig. 2e. When subjected to an external magnetic field at 1.7 K, the electrical resistance of single-crystal Cu_3BHT increases by approximately 2%, consistent with ordinary magnetoresistance[41]. This response can be attributed to the magnetic field's effect on electron motion within the lattice, which leads to increased scattering events and, consequently, higher overall resistance. Additionally, ultraviolet photoelectron spectroscopy (UPS) analysis indicates that the Fermi level of Cu_3BHT intersects with the conduction band, as illustrated in Fig. 2f, providing additional support for the material's metallic behavior.

Superconductivity characterization and magnetic properties

To investigate the Cu_3BHT crystal's magnetic properties, magnetization measurements were performed under applied magnetic fields ranging from 0 to 5 T at various temperatures. The resulting curves consistently demonstrate paramagnetic characteristics across these temperatures (Fig. 3a). As shown in Fig. 3b, no divergence was observed between the temperature dependence of magnetic susceptibilities collected from zero-field-cooled (ZFC) and field-cooled (FC) measurements, indicating the absence of long-range magnetic ordering down to at least 2 K. The temperature dependence of

https://doi.org/10.1038/s41467-024-53786-1

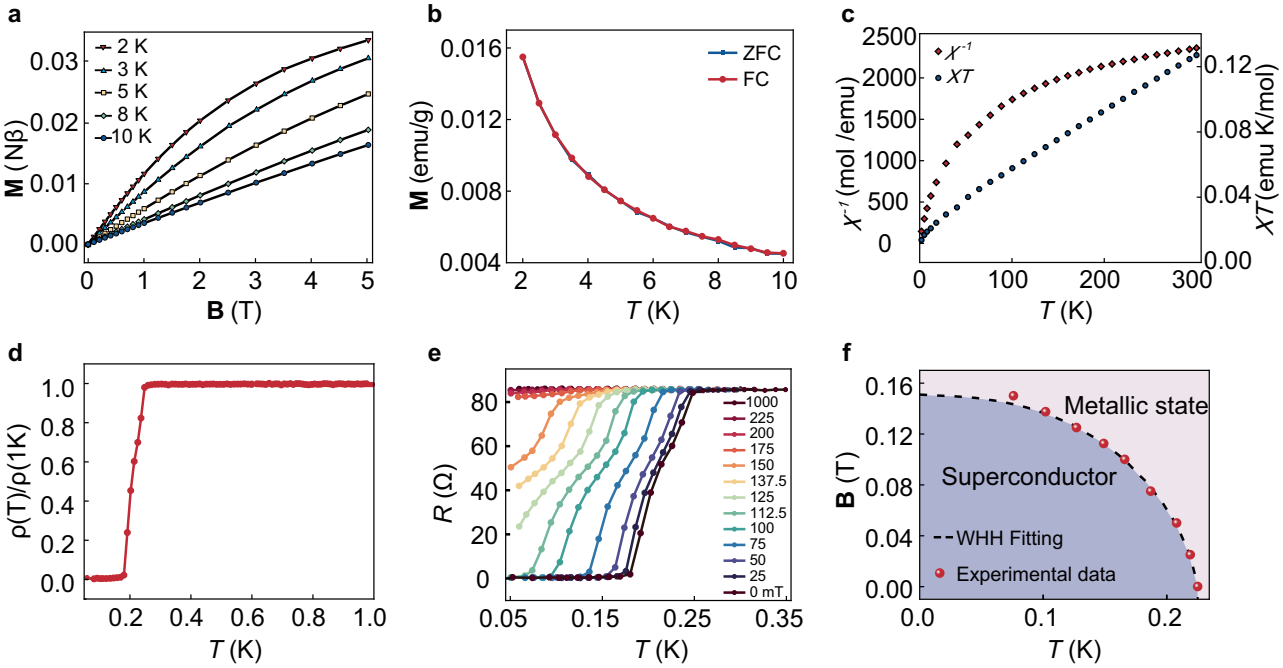

Fig. 3 | Superconductivity and magnetic properties of Cu_3BHT 2. a The relationship between magnetization and magnetic fields under different temperatures. **b** Zero-field-cooling curve and field-cooling curve of Cu_3BHT. **c** Temperature dependence of magnetic susceptibility and inverse susceptibility. **d** The temperature dependence of normalized resistance. **e** The variation of resistance with temperature under an applied magnetic field parallel to the *ab* plane ranging from 0 to 1000 mT. **f** The phase diagram of superconductivity.

magnetic susceptibility, $\chi(T)$, was examined under a 500 mT magnetic field. The inverse susceptibility, $\chi^{-1}(T)$, was also calculated and is presented in Fig. 3c. The susceptibility and its inverse curve clearly follow Curie's law, further supporting the non-Fermi liquid behavior[42]. These magnetic characterizations collectively confirm the paramagnetic nature of Cu_3BHT down to at least 2 K. Moreover, χT at 300 K is approximately 0.125 emu K/mol, corresponding to an effective moment of $\mu_{eff} = 0.577\mu_B$. This value is roughly one-third of the expected value for Cu^{2+} ions with $S = 1/2$ ($\mu_{eff} = 1.73\mu_B$). This suggests that approximately one-third of the Cu atoms in Cu_3BHT should be Cu^{2+}. The temperature dependence of the direct current (DC) magnetic susceptibility for Cu_3BHT microcrystals from different batches is in excellent agreement, thereby confirming the reproducibility of their magnetic properties (Supplementary Fig. 18). This conclusion is further supported by *X*-ray photoelectron spectroscopy (XPS) analysis (Supplementary Fig. 19), which indicates that both Cu^+ and Cu^{2+} exist in Cu_3BHT with a ratio of approximately 2:1. Combined with the crystal structure analysis, it is suggested that Cu^{2+} ions are associated with a square pyramidal structure, while Cu^+ ions adopt a square planar coordination geometry. These results also suggest that copper exhibits mixed valence in Cu_3BHT, with the total anionic charge of BHT being −4. The mixed valence of copper in Cu_3BHT may be caused by metal-to-ligand charge transfer rather than the involvement of an external oxidizing agent. When Cu^{2+} is reduced to Cu^+, the ligand is oxidized to a −4 state. Since three equivalents of Cu^{2+} and one equivalent of BHT^{6-} participate in the reaction, the result is a net zero charge. Even when charge transfer occurs between the copper and the ligand, the result is a net zero charge.

In the Cu_3BHT crystal, a sharp decline in resistance is observed as the temperature drops to 0.25 K, signaling the onset of superconductivity. The superconducting transition is highly abrupt, with a transition width ΔT_c of 40 mK, which is significantly smaller than the transition temperature (Fig. 3d). Furthermore, additional devices exhibit superconducting transitions, though with slight variations in transition temperature and ΔT_c, likely arising from differences in crystal and device quality (Supplementary Fig. 20). The close agreement in transition temperature between the examined Cu_3BHT crystal and the thin film sample suggests that both host the same superconducting phase, further highlighting the intrinsic characteristics and reproducibility of the material. In the magnetic field range of 0 to 1 T applied along the *ab* plane and the supercurrent flowing along the *c*-axis, the superconducting critical temperature (T_c) shifts toward lower temperatures as the magnetic field strength increases (Fig. 3e). At a magnetic field of 1 T, the superconductivity completely vanishes. By employing the Werthamer–Helfand–Hohenberg (WHH) formula[43], the critical magnetic field at zero temperature for Cu_3BHT is determined to be 0.15 T (Fig. 3f), and the superconducting coherence length is computed as 47 nm using the expression $\xi_0 = [\Phi_0/2\pi H_{c2}[0])]^{0.5}$. This relatively large coherence length is significantly smaller than the sample diameter (~200 nm), indicating the presence of bulk superconductivity.

Band structure calculation

Density functional theory (DFT) electronic band structure calculation was conducted based on the atomic-precise crystal structure of Cu_3BHT, revealing its inherent metallic properties (Fig. 4a and Supplementary Fig. 21), which is in good agreement with UPS results. At the Fermi level, notable contributions to the density of state (DOS) stem from the *d* orbitals of Cu, as well as the *p* orbitals of S and C (Supplementary Fig. 22), indicating a pronounced degree of conjugation within the material. The electron band structure of Cu_3BHT is depicted along the high-symmetry points of the first Brillouin zone (Fig. 4b), revealing prominent bands crossing the Fermi level along several directions, including Γ–M, Γ–A, A–M, M–B, Γ–B, and Z–D, indicating its metallic properties within the plane. Moreover, particular emphasis is placed on the material's metallic characteristics extending into the *c* direction, as demonstrated by the band crossings at the Fermi level in the out-of-plane directions Γ–Z and B–D. The in-plane metallic behavior arises from the conductive pathway of π–*d* conjugation interactions between transition metal *d* orbitals and organic

https://doi.org/10.1038/s41467-024-53786-1

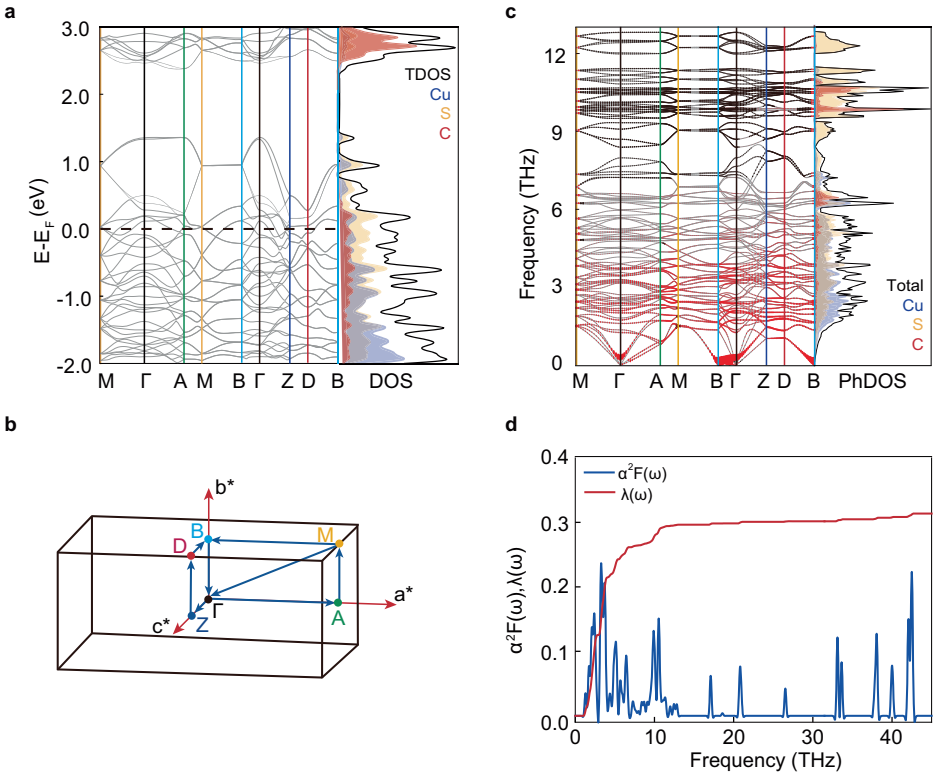

Fig. 4 | Electronic band structure and phonon spectrum of Cu_3BHT. a Electronic band structure and DOS of Cu_3BHT. **b** Corresponding first Brillouin zone and high-symmetry K-points. **c**, Phonon spectrum with the EPC λ_{qv} indicated by red circles, with the size of each circle being proportional to the magnitude of λ_{qv}. **d** Eliashberg spectral function $\alpha^2F(\omega)$ and cumulative frequency-dependent $\lambda(\omega)$.

ligand π orbitals, with the kagome structure formed by densely connected square pyramidal Cu atoms and BHT ligands. In the *c* direction, the metallicity predominantly arises from interlayer Cu–S bonds formed by pentacoordinate Cu atoms and adjacent S atoms, which play a more significant role than van der Waals interactions, significantly enhancing perpendicular conductivity.

The phonon spectrum and density of states for various atoms (Fig. 4c), along with the Eliashberg spectral function and the cumulative frequency function of the electron–phonon coupling (EPC) strength in Cu_3BHT (Fig. 4d), indicate pronounced EPC at frequencies below 6 THz, where phonons are predominantly contributed by the vibrations of Cu and S atoms. Specifically, the coordination of square pyramidal Cu atoms with S atoms within layers and the coordination of pentacoordinate Cu atoms with S atoms from adjacent layers, play a major role. The Cu–S bonds not only enhance electron–electron interactions within and between layers but also strengthen electron–phonon coupling, significantly contributing to the material's superconducting properties. This underscores the importance of interlayer Cu–S bonding along the π–π stacking direction and provides new insights into the out-of-plane structural characteristics of kagome superconductors. Furthermore, the vibrational coupling between S and C atoms at frequencies around 10 THz indicates strong in-plane EPC, whereas the high-frequency stretching vibrations of C atoms at frequencies above 30 THz contribute relatively less to the overall EPC strength (Supplementary Fig. 23). By unfolding the electronic band structures to the Brillouin zone of the kagome lattice formed by Cu atoms within Cu_3BHT, characteristic features of a kagome band structure are observed, including the Dirac cone at the corners of the Brillouin zone, a van Hove singularity at the zone boundary center, and a flat band extending across the entire Brillouin zone (Supplementary Fig. 24). Despite the presence of hybridized gaps resulting from interactions between the kagome bands and other metallic bands, this exploration has the potential to uncover a wealth of emergent quantum phenomena, which are profoundly significant for discovering and understanding of new kagome superconductors.

The Cu_3BHT structure achieves superconductivity through unique mechanisms that enhance both electron–electron interactions and electron–phonon coupling. This structure features a layered arrangement where organic ligands and metal ions create π–*d* conjugated conductive pathways within an exceptionally dense kagome lattice. The interlayer connectivity is further augmented by pentadentate Cu atoms, which form Cu–S bonds with S atoms from adjacent layers, thereby shortening electron transport distances, increasing electron density, and avoiding Peierls distortion. These features significantly amplify electron–electron interactions. The primary contributors to electron–phonon coupling in Cu_3BHT are the Cu and S atoms, along with the plane's S and C atoms. Interlayer Cu–S bonds further enhance electron–phonon coupling effects in this material. The unique kagome lattice structure and interlayer Cu–S bonds collectively optimize these properties, distinguishing Cu_3BHT's superconductivity from other organic–inorganic hybrid materials.

Discussion

In summary, our study, for the first time, achieved the atomic-precise crystal structure analysis of Cu_3BHT, showcasing a unique non-van der Waals 2D structure characterized by strong interlayer interactions through Cu–S covalent bonds. Single-crystal devices of Cu_3BHT oriented in the out-of-plane direction exhibited a complex metallic behavior and a superconducting transition at 0.25 K. DFT calculations indicate that the covalently bonded intralayer structure enhances electron–electron interactions and electron–phonon coupling, contributing to the observed properties. These findings deepen the understanding of crystal packing structure and electrical properties of c-CP materials, thus paving the way for the design of other c-CP-based

metallic and superconducting materials. These materials will be anticipated to have a substantial impact on the development of c-CP-based quantum devices.

Methods

Materials

$CuCl_2$ was purchased from Alfa Aesar China (Tianjin) Co., Ltd. Toluene was purchased from Beijing Yili Fine Chemicals Co. Ltd. Water was purified using the Milli-Q purification system. Both solvents were degassed by Freeze–Thaw method before use. Benzenehexathiol (BHT) was synthesized according to the literatures[44]. All the processing solvents, including ultra-dry methanol, ultra-dry ethanol, acetone, methyl isobutyl ketone (MIBK), polymethyl methacrylate, and methyl methacrylate, were purchased from commercial sources and used as received. All commercially available chemicals were used without further purification unless otherwise noted. All air- and water-sensitive reactions were performed under a nitrogen atmosphere.

Micro-ED data collection and procession of Cu_3BHT

The sample powder was finely pulverized using an agate mortar, then dispersed in pure ethanol and ultrasonicated for 2 min to ensure even distribution. A small amount of this dispersion was then carefully placed onto a copper grid, which had been prepared with a holey carbon film. The specimen underwent Micro-ED analysis using a JEOL JEM2100 transmission electron microscope (TEM) operating at 200 kV. This microscope was fitted with a Timepix pixel detector by Amsterdam Scientific Instruments. To reduce the risk of beam-induced damage, the specimen was cooled to 96 K using a Gatan cryo-transfer tomography holder before the start of data collection. A Cu_3BHT crystal was then positioned within the electron beam and aligned to the correct mechanical eucentric height. Throughout the data collection phase, the goniometer was in constant rotation, capturing selected-area Electron Diffraction patterns from the crystal at a spot size of 3 with 0.5 s exposure times for each pattern.

Structure determination of Cu_3BHT

The final unit cell parameters were refined using synchrotron powder X-ray diffraction (SPXRD) through Pawley fitting, which determined the parameters to be $a = 14.8082(10)$ Å, $b = 8.6706(6)$ Å, $c = 6.8357(5)$ Å, with the angles $\alpha = \gamma = 90°$ and $\beta = 97.342(2)°$. Following this, ab initio structure solution of the merged 3D Electron Diffraction (ED) data was conducted using superflip software. This process successfully identified all non-hydrogen atoms within the space group $P2_1/c$ for the preliminary structural model. The final structural refinement was carried out using Jana20065, employing the unit cell parameters obtained from SPXRD.

Powder X-ray Diffraction (PXRD) analyses were performed using a Panalytical Rigaku D X-ray powder diffractometer, utilizing Cu Kα radiation ($\lambda = 1.5406$ Å) from a D/max 2500 source and Shanghai synchrotron radiation light source ($\lambda = 0.458086$ Å). Measurements covered a 2θ range from 5° to 60°, with a step increment of 0.023° and an exposure duration of 60 s for each step.

Scanning electron microscopy (SEM) studies were conducted on an FEI Quattro S instrument, operating across an acceleration voltage range of 5 to 30 kV. Given the excellent conductivity of Cu_3BHT, the process did not necessitate any supplementary metal coating.

High-resolution transmission electron microscopy (HRTEM) images were captured using a JEOL 2100F transmission electron microscope at an acceleration voltage of 120 kV.

Cryo-electron microscopy (cryo-EM) study was performed on an FEI Titan Krios TEM (Gatan K2 summit camera) operated at 300 kV with a GIF Quantum energy filter (Gatan).

High-resolution scanning transmission electron microscopy (STEM) images were produced with a Nion UltraSTEM 100 microscope, featuring a spherical aberration corrector and an operational voltage of 60 kV.

Ultraviolet photoelectron spectroscopy (UPS) and X-ray photoelectron spectroscopy (XPS) were performed using the Kratos AXIS Ultra Photoelectron Spectrometer. The measurements were conducted under ultra-high vacuum conditions (3×10^{-9} Torr). The excitation sources used are He I (21.11 eV) and monochromatic light source Al Kα (1486.6 eV). All binding energy values displayed were calibrated to the C1s peak at 284.8 eV, and data analysis was carried out using the Avantage software.

Raman spectroscopy was conducted using a Horiba spectrometer with 532 nm laser excitation to investigate the structural properties of Cu_3BHT.

Device fabrication

Initially, Cu_3BHT was ultrasonically dispersed in methanol, the dispersion was meticulously applied onto a pre-defined Si/SiO_2 substrate via a spin-coating process to ensure solvent evaporation and the uniform distribution of single crystals. Following this, the substrate was coated with MMA and PMMA, which were then subjected to thermal annealing at temperatures of 150 °C and 170 °C for a duration of two minutes, respectively. Utilizing a 30 kV electron beam, lithographic patterning was conducted, with MIBK serving as the developer for the exposed patterns. This was succeeded by the deposition of a 5 nm titanium layer and a 250 nm gold layer through the process of magnetron sputtering. The fabrication sequence was finalized with a lift-off process in acetone, culminating in the preparation of the device.

Variable temperature electrical conductivity data of single crystals using autocube attoDRY 2100 with SR830 Lock-In Amplifier. Single crystal devices were bonded to chips of attoDRY 2100 with aluminum wire using WestBond 7476D wire bonder.

Magnetic properties were assessed using a Quantum Design Dynacool D-209 Physical Property Measurement System (PPMS). These measurements of susceptibility were conducted in an external field of 500 mT across temperatures from 1.7 to 300 K. The data were then adjusted to account for the diamagnetic effects, using both measurements from a blank sample holder and Pascal's constants for correction.

The superconductivity measurements over a temperature range of 0.05 to 1 K were performed using a Quantum Design PPMS DynaCool system equipped with an Electrical Transport Option. In a custom four-contact probe cell, copper wires were affixed to the sample puck's copper current collector.

The superconductivity of Cu_3BHT was estimated based on the calculation of electronic propriety, phonon spectrum, and EPC strength within the framework of DFT[45,46] and density-functional perturbation theory[47], which is implemented in the QE package[48]. The generalized gradient approximation (GGA) in the functional type of Perdew–Burke–Ernzerh (PBE)[49] was employed for the ultrasoft pseudopotentials, and the cutoff energy was set to 80 Ry for wave functions and 640 Ry for charge density. During structural relaxation and self-consistent calculations, the Gaussian spreading value of 0.01 Ry was employed for the method of Methfessel–Paxton first-order spreading to determine electron occupations under the uniform $4 \times 2 \times 4$ **k**-point mesh. The dynamic matrix and phonon frequency were computed on a $1 \times 1 \times 1$ **q**-point mesh with a $4 \times 2 \times 4$ **k**-point sampling in the Brillouin zone of Cu_3BHT, and a finer $8 \times 4 \times 8$ **k**-point grid is used for the EPC calculations. The cumulative frequency-dependent $\lambda(\omega)$ was calculated from the Eliashberg spectral function $\alpha^2F(\omega)$ via the formula $\lambda(\omega) = 2\int_0^{\omega} d\omega' \frac{\alpha^2F(\omega')}{\omega'}$. The total EPC λ corresponds to the value of $\lambda(\omega_{max})$ with the ω_{max} being the maximum of phonon frequency. The superconducting transition temperature was envaulted from the McMillan–Allen–Dynes (MAD) $T_C = \frac{\omega_{log}}{1.2} \exp\left[\frac{-1.04 \times (1+\lambda)}{\lambda - \mu^* \times (1+0.62 \times \lambda)}\right]$[50,51]. Here the Coulomb pseudopotential μ^* is set to 0.1 and the logarithmically averaged frequency ω_{log} is defined by $\omega_{log} = \exp\left[\frac{2}{\lambda}\int_0^{\infty} \frac{\alpha^2F(\omega)}{\omega} \ln\omega d\omega\right]$.

The Vienna Ab initio Simulation Package (VASP)[52] was employed to unfolding electronic band structures to the Brillouin zone of kagome lattice formed by the Cu atoms within Cu_3BHT, where the GGA-PBE[49] and projector augmented wave pseudopotentials[53] with the energy cutoff of 500 eV were used.

Data availability

Crystallographic data for the structures reported in this Article have been deposited at the Cambridge Crystallographic Data Center under deposition number CCDC 12381830. Copies of the data can be obtained free of charge via https://www.ccdc.cam.ac.uk/structures/. The data supporting our findings are included in the article and supplementary files. Additional data generated during the study are available from the corresponding author upon request. Source data are provided in this paper.

References

1. Givaja, G., Amo-Ochoa, P., Gómez-García, C. J. & Zamora, F. Electrical conductive coordination polymers. *Chem. Soc. Rev.* **41**, 115–147 (2012).
2. Wang, M. C., Dong, R. H. & Feng, X. L. Two-dimensional conjugated metal-organic frameworks (2D c-MOFs): chemistry and function for MOFtronics. *Chem. Soc. Rev.* **50**, 2764–2793 (2021).
3. Xie, L. S., Skorupskii, G. & Dinca, M. Electrically conductive metal-organic frameworks. *Chem. Rev.* **120**, 8536–8580 (2020).
4. Li, H., Eddaoudi, M., O'Keeffe, M. & Yaghi, O. M. Design and synthesis of an exceptionally stable and highly porous metal-organic framework. *Nature* **402**, 276–279 (1999).
5. Talin, A. A. et al. Tunable electrical conductivity in metal-organic framework thin-film devices. *Science* **343**, 66–69 (2014).
6. Dou, J. H. et al. Atomically precise single-crystal structures of electrically conducting 2D metal-organic frameworks. *Nat. Mater.* **20**, 222–228 (2021).
7. Feng, D. W. et al. Robust and conductive two-dimensional metal-organic frameworks with exceptionally high volumetric and areal capacitance. *Nat. Energy* **3**, 30–36 (2018).
8. Huang, X. et al. A two-dimensional *π-d* conjugated coordination polymer with extremely high electrical conductivity and ambipolar transport behaviour. *Nat. Commun.* **6**, 7408 (2015).
9. Huang, X. et al. Highly conducting neutral coordination polymer with infinite two-dimensional silver-sulfur networks. *J. Am. Chem. Soc.* **140**, 15153–15156 (2018).
10. Huang, X. et al. Superconductivity in a copper(II)-based coordination polymer with perfect kagome structure. *Angew. Chem. Int. Ed.* **57**, 146–150 (2018).
11. Kambe, T. et al. Redox control and high conductivity of nickel bis(dithiolene) complex π-nanosheet: a potential organic two-dimensional topological insulator. *J. Am. Chem. Soc.* **136**, 14357–14360 (2014).
12. Liu, J. X. et al. On-liquid-gallium surface synthesis of ultrasmooth thin films of conductive metal-organic frameworks. *Nat. Synth.* **3**, 715–726 (2024).
13. Dou, J. H. et al. Signature of metallic behavior in the metal-organic frameworks M_3(hexaiminobenzene)$_2$ (M = Ni, Cu). *J. Am. Chem. Soc.* **139**, 13608–13611 (2017).
14. Park, J. et al. Stabilization of hexaaminobenzene in a 2D conductive metal-organic framework for high power sodium storage. *J. Am. Chem. Soc.* **140**, 10315–10323 (2018).
15. Skorupskii, G. et al. Efficient and tunable one-dimensional charge transport in layered lanthanide metal-organic frameworks. *Nat. Chem.* **12**, 131–136 (2020).
16. Day, R. W. et al. Single crystals of electrically conductive two-dimensional metal-organic frameworks: structural and electrical transport properties. *ACS Cent. Sci.* **5**, 1959–1964 (2019).
17. Hmadeh, M. et al. New porous crystals of extended metal-catecholates. *Chem. Mat.* **24**, 3511–3513 (2012).
18. Sheberla, D. et al. Conductive MOF electrodes for stable supercapacitors with high areal capacitance. *Nat. Mater.* **16**, 220–224 (2017).
19. Miner, E. M. et al. Electrochemical oxygen reduction catalysed by Ni_3(hexaiminotriphenylene)$_2$. *Nat. Commun.* **7**, 10942 (2016).
20. Sheberla, D. et al. High electrical conductivity in Ni_3(2,3,6,7,10,11-hexaiminotriphenylene)$_2$, a semiconducting metal-organic graphene analogue. *J. Am. Chem. Soc.* **136**, 8859–8862 (2014).
21. Dong, R. et al. High-mobility band-like charge transport in a semiconducting two-dimensional metal-organic framework. *Nat. Mater.* **17**, 1027–1032 (2018).
22. Banda, H., Dou, J. H., Chen, T. Y., Zhang, Y. G. & Dinca, M. Dual-ion intercalation and high volumetric capacitance in a two-dimensional non-porous coordination polymer. *Angew. Chem. Int. Ed.* **60**, 27119–27125 (2021).
23. Zhu, B. J., Wen, D. S., Liang, Z. B. & Zou, R. Q. Conductive metal-organic frameworks for electrochemical energy conversion and storage. *Coord. Chem. Rev.* **446**, 214119 (2021).
24. Kambe, T. et al. π-Conjugated nickel bis(dithiolene) complex nanosheet. *J. Am. Chem. Soc.* **135**, 2462–2465 (2013).
25. Zhang, L. Z. et al. Intrinsic two-dimensional organic topological insulators in metal-dicyanoanthracene lattices. *Nano Lett.* **16**, 2072–2075 (2016).
26. Wang, Z. F., Liu, Z. & Liu, F. Organic topological insulators in organometallic lattices. *Nat. Commun.* **4**, 1471 (2013).
27. Lin, L. et al. Lattice strained induced spin regulation in Co-N/S coordination-framework enhanced oxygen reduction reaction. *Angew. Chem. Int. Ed.* **63**, 202319518 (2024).
28. Misumi, Y. et al. Quantum spin liquid state in a two-dimensional semiconductive metal-organic framework. *J. Am. Chem. Soc.* **142**, 16513–16517 (2020).
29. Galeotti, G. et al. Synthesis of mesoscale ordered two-dimensional π-conjugated polymers with semiconducting properties. *Nat. Mater.* **19**, 874–880 (2020).
30. Takenaka, T. et al. Strongly correlated superconductivity in a copper-based metal-organic framework with a perfect kagome lattice. *Sci. Adv.* **7**, eabf3996 (2021).
31. Zhang, X. M., Zhou, Y. N., Cui, B., Zhao, M. W. & Liu, F. Theoretical discovery of a superconducting two-dimensional metal-organic framework. *Nano Lett.* **17**, 6166–6170 (2017).
32. Fan, K., Zhang, C. Y., Chen, Y., Wu, Y. C. & Wang, C. L. The chemical states of conjugated coordination polymers. *Chemistry* **7**, 1224–1243 (2021).
33. Han, J. L. et al. Determining factors in the growth of MOF single crystals unveiled by in situ interface imaging. *Chemistry* **8**, 1637–1657 (2022).
34. Howarth, A. J. et al. Best practices for the synthesis, activation, and characterization of metal-organic frameworks. *Chem. Mat.* **29**, 26–39 (2017).
35. Tang, K. L., Jin, X. L., Long, Y. L., Cui, P. & Tang, Y. Q. Study on the reaction of the anionic copper selenolate complex $[Me_4N]_2[Cu_4(SePh)_6]$ with CS_2 in solvents: the crystal structure of a polymeric complex $[CuS_2COMe]_n$(I). *J. Chem. Res.* **9**, 452–453 (2000).
36. Valigura, D., Ondrejovic, G. & Kratsmarsmogrovic, J. Space orientation and bonding properties of thiourea in *N*-salicylideneglycinatocopper(II) complex. *Chem. Pap.* **41**, 183–193 (1987).
37. Radisavljevic, B. & Kis, A. Mobility engineering and a metal-insulator transition in monolayer MoS_2. *Nat. Mater.* **12**, 815–820 (2013).
38. Denoyer, F., Comes, F., Garito, A. F. & Heeger, A. J. X-ray-diffuse-scattering evidence for a phase transition in tetrathiafulvalene tetracyanoquinodimethane (TTF-TCNQ). *Phys. Rev. Lett.* **35**, 445–449 (1975).

39. Fickett, F. R. Oxygen-free copper at 4K-resistance and magnetoresistance. *IEEE Trans. Magn.* **19**, 228–231 (1983).
40. Das, P., Saha, P., Singh, M., Kumar, P. & Patnaik, S. Quantum linear magnetoresistance and fermi liquid behavior in Kagome Metal $Ni_3In_2S_2$. Preprint at *arXiv* https://doi.org/10.48550/arXiv.2402.10096 (2024).
41. Ross, A. et al. Structural sensitivity of the spin Hall magnetoresistance in antiferromagnetic thin films. *Phys. Rev. B* **102**, 094415 (2020).
42. Löhneysen, H. v. et al. Non-Fermi-liquid behavior in a heavy-fermion alloy at a magnetic instability. *Phys. Rev. Lett.* **72**, 3262–3265 (1994).
43. Werthamer, N. R., Helfand, E. & Hohenberg, P. C. Temperature and purity dependence of the superconducting critical field, H_{c2}. III. electron spin and spin-orbit effects. *Phys. Rev.* **147**, 295–302 (1965).
44. Yip, H. K., Schier, A., Riede, J. & Schmidbaur, H. Benzenehexathiol as a template rim for a golden wheel: synthesis and structure of $[\{CSAu(PPh_3)\}_6]$. *J. Chem. Soc. Dalton Trans.* **15**, 2333–2334 (1994).
45. Hohenberg, P. & Kohn, W. Inhomogeneous electron gas. *Phys. Rev. B* **136**, B864–B871 (1964).
46. Kohn, W. & Sham, L. J. Self-consistent equations including exchange and correlation effects. *Phys. Rev.* **140**, A1133–A1138 (1965).
47. Baroni, S., de Gironcoli, S., Dal Corso, A. & Giannozzi, P. Phonons and related crystal properties from density-functional perturbation theory. *Rev. Mod. Phys.* **73**, 515–562 (2001).
48. Giannozzi, P. et al. Quantum ESPRESSO toward the exascale. *J. Chem. Phys.* **152**, 154105 (2020).
49. Perdew, J. P., Burke, K. & Ernzerhof, M. Generalized gradient approximation made simple. *Phys. Rev. Lett.* **78**, 1396–1396 (1997).
50. McMillan, W. L. Transition temperature of strong-coupled superconductors. *Phys. Rev.* **167**, 331–344 (1968).
51. Allen, P. B. & Dynes, R. C. Transition temperature of strong-coupled superconductors reanalyzed. *Phys. Rev. B* **12**, 905–922 (1975).
52. Kresse, G. & Furthmuller, J. Efficiency of ab-initio total energy calculations for metals and semiconductors using a plane-wave basis set. *Comput. Mater. Sci.* **6**, 15–50 (1996).
53. Blochl, P. E. Projector augmented-wave method. *Phys. Rev. B* **50**, 17953–17979 (1994).

Acknowledgements

This work was financially supported by the National Key R&D Program of China (Grant No. 2023YFE0206400), the National Natural Science Foundation of China (Grant No. 22171185, No. 12488201), and the Clinical Medicine Plus X-Young Scholars Project at Peking University, backed by the Fundamental Research Funds for the Central Universities. The staff of beamlines BL17B1, BL14B1, and BL18U1 of the National Facility for Protein Science Shanghai (NFPS) at the Shanghai Synchrotron Radiation Facility (SSRF) are acknowledged for their assistance in the data collection. We appreciate the Molecular Materials and Nanofabrication Laboratory (MMNL) in the College of Chemistry and Electron Microscopy Laboratory of Peking University for the support of instruments to perform device fabrication and characterization. Cryo-EM data were collected on the Electron Microscopy Laboratory of Peking University with the assistance. Thanks to Ms. Li Xuemei for her help in sample preparation and data collection. X.Z. acknowledges financial support from the National Natural Science Foundation of China (No. 12004357). Thanks to Dr. Yigang Jin for his help in the powder refinement of the PXRD date of BHT. Thanks to Ze Li, Sha Wu, and Xinyu Wang for conducting the IR and Raman spectroscopy measurements. S.W. and L.S. acknowledge financial support from the Zhejiang Provincial Natural Science Foundation of China (Grant No. XHD23B0301) and the Research Center for Industries of the Future (RCIF Project No. WU2023C006) as well as thank Dr. Chao Zhang, Yingchao Wang, and the Instrumentation and Service Center for Material Sciences at Westlake University for the support with the electrical characterization. We sincerely appreciate Qingqing Ji, Jingyue Wang, and Yue Lu for their helpful discussion.

Author contributions

J.D., Z.P., and X.H. conceived the idea and designed the experiments. X.H. synthesized the samples. J.L. and W.X. conducted the structural analysis. Z.P., Y.F. X.C., and T.Z. performed the material investigations, fabricated single crystal devices, and conducted the electrical measurements. X.Z. performed the DFT calculations of superconductivity and electronic property. S.W., S.Q., L.S., and J.W. conducted the magnetic and superconductivity performance tests. Y.L. and Y.X. performed the fitting of the superconducting phase diagram. Z.P., X.H., Y.F., Y.Z., and J.D. analyzed the experimental data and wrote the main manuscript. J.D. supervised the entire project. All authors contributed to the data analysis and provided feedback on the manuscript.

Competing interests

The authors declare no competing interests.

Additional information

Supplementary information The online version contains supplementary material available at https://doi.org/10.1038/s41467-024-53786-1.

Correspondence and requests for materials should be addressed to Jin-Hu Dou.

Peer review information *Nature Communications* thanks Carlos Gómez-García, Hiroshi Nishihara, and Takasada Shibauchi for their contribution to the peer review of this work. A peer review file is available.